HHS Public Access

Author manuscript

Nature. Author manuscript; available in PMC 2018 June 06.

Published in final edited form as:

Nature. 2017 December 14; 552(7684): 205–209. doi:10.1038/nature24997.

Structures of the Calcium-activated Non-Selective Cation Channel TRPM4

Jiangtao Guo[1,2,*], **Ji She**[1,2,*], **Weizhong Zeng**[1,2,3], **Qingfeng Chen**[1,2,3], **Xiao-chen Bai**[2,#], and **Youxing Jiang**[1,2,3,#]

[1]Department of Physiology, University of Texas Southwestern Medical Center, Dallas, Texas 75390-9040

[2]Department of Biophysics, University of Texas Southwestern Medical Center, Dallas, Texas 75390-8816

[3]Howard Hughes Medical Institute, University of Texas Southwestern Medical Center, Dallas, Texas 75390-9040

Abstract

TRPM4 is a calcium-activated, phosphatidylinositol bisphosphate ($PtdInsP_2$) modulated, non-selective cation channel, and belongs to the family of melastatin-related transient receptor potential (TRPM) channels. Here we present the cryo-EM structures of the mouse TRPM4 channel with and without ATP. TRPM4 consists of multiple transmembrane and cytosolic domains, which assemble into a three-tiered architecture. The N-terminal nucleotide binding domain (NBD) and the C-terminal coiled coil participate in the tetrameric assembly of the channel; ATP binds at NBD and inhibits channel activity. TRPM4 has an exceptionally wide filter but is only permeable to monovalent cations; filter residue Gln973 is essential in defining monovalent selectivity. S1-S4 domain and post-S6 TRP domain form the central gating apparatus that likely house the Ca^{2+} and $PtdInsP_2$ binding sites. These structures provide an essential starting point for elucidating the complex gating mechanisms of TRPM4 and also reveal the molecular architecture of the TRPM family for the first time.

Introduction

The melastatin-related transient receptor potential (TRPM) channels comprise the largest subfamily of TRP channels and have diverse functions in various physiological processes[1–3].

[#]**Address correspondence to**: Youxing Jiang, Ph.D., Department of Physiology, UT Southwestern Medical Center, 5323 Harry Hines Blvd., Dallas, Texas 75390-9040, Tel. 214 645-6027; Fax. 214 645-6042; youxing.jiang@utsouthwestern.edu; Xiaochen Bai, Ph.D., Department of Biophysics, UT Southwestern Medical Center, 5323 Harry Hines Blvd., Dallas, Texas 75390-8816, Tel. 214 648-6089; xiaochen.bai@utsouthwestern.edu.

[*]These authors contributed equally.

The authors declare no competing financial interests.

Author Contributions J.G. and J.S. prepared the samples; J.G., J.S., Q.C. and X.B. performed data acquisition, image processing and structure determination; W.Z. performed electrophysiology; all authors participated in research design, data analysis, and manuscript preparation.

TRPM channels share a conserved N-terminal cytosolic region of about 700 amino acid residues with uncharacterized structure and function. At the C-terminal region, TRPM channels contain the TRP domain followed by a coiled coil domain[1]. Some TRPM channels such as TRPM2, 6 and 7 have functional enzyme domains at the C-terminus and therefore are called chanzymes (channel + enzyme)[4–6]. Among the eight members of the TRPM subfamily, TRPM4 and TRPM5 share high sequence homology (about 50% identity) and similar biophysical properties such as ligand regulation, voltage-dependency, ion selectivity and single-channel conductance[7]. Both channels conduct the calcium-activated non-selective cationic (NSC_{Ca}) current first recorded in cardiac tissues[8]. Distinct from other TRP channels, TRPM4 and TRPM5 are impermeable to divalent cations such as Ca^{2+} and Mg^{2+} (ref. [7]). While TRPM4 is ubiquitously expressed in pancreas, heart, prostate, renal tubule and many other tissues and organs[9,10], TRPM5 is mainly detected in taste receptor cells[11].

TRPM4 is regulated by multiple cellular stimuli[3,7,12] (Extended Data Fig. 1). Upon Ca^{2+} activation, TRPM4 is desensitized to a steady state within a minute at both negative and positive membrane potentials. This TRPM4 desensitization was attributed to the loss of phosphatidylinositol 4,5-bisphosphate (PtdIns(4,5)P_2) in the membrane due to Ca^{2+}-activated phospholipase C[13,14]. At the Ca^{2+}-desensitized steady state, TRPM4 exhibits voltage-dependent gating with higher channel open probability at depolarizing membrane potential[10]. While PtdInsP_2 alone cannot activate the channel, its presence with Ca^{2+} reverses channel desensitization, potentiates Ca^{2+} sensitivity, and mitigates voltage dependence of the channel[13,14]. Cytosolic ATP can modulate TRPM4 activity in a seemingly paradoxical manner – it inhibits TRPM4 current but can also reverse Ca^{2+} desensitization[13,15,16].

TRPM4 activation can depolarize the plasma membrane potential and activate voltage-gated sodium or calcium channels[7]. Thus, its function has been implicated in many important physiological processes including the Bayliss effect in cerebral arteries in response to stretch[17,18], the breath pacemaking in brainstem neurons[19,20], the insulin secretion of pancreatic β cells in response to glucose uptake[21], and the Ca^{2+}-dependent immune response in T lymphocytes and dendritic cells[22]. In cardiac cells, several mutations in TRPM4 were found to be associated with human heart conduction dysfunction[23–27]. Despite of its physiological importance, the lack of structural information about TRPM4 as well as other members of TRPM family hampers our understanding of the complex regulation of TRPM4. In this study, we determined the structures of the mouse TRPM4 channel by single-particle electron cryo-microscopy (cryo-EM), revealing the unique molecular architecture of the TRPM family. Along with electrophysiological analysis, we also elucidated the structural basis of ATP modulation and ion selectivity in TRPM4 channel.

Results

Overall structure of TRPM4

The mouse TRPM4 was purified and reconstituted into nanodiscs and its structures in the apo and ATP-bound states were determined by cryo-EM to a resolution of 3.1 and 2.9 Å, respectively, using the gold-standard Fourier shell correlation (FSC) = 0.143 criteria[28] (Extended Data Fig. 2–6 and Methods). The cryo-EM density maps are of sufficient quality

for model building of major parts of the protein (Extended Data Fig 5). Both structures represent the closed state and are highly similar except for the nucleotide binding region, as will be discussed later. The EM map for apo TRPM4 is of better quality at the peripheral region, therefore the apo structure will be used in most of the discussion.

The homotetrameric TRPM4 channel has a molecular weight of about 500 kDa with dimensions of 150 × 100 × 100 Å (Fig. 1a and b). Each TRPM4 subunit contains multiple cytosolic domains and the overall architecture of the channel tetramer can be divided into three tiers (Fig. 1b–d). The bottom tier consists of the N-terminal nucleotide binding domain (NBD), the ankyrin repeat domain (ARD) and the C-terminal coiled-coil helix, all of which participate in the tetrameric assembly of the channel. The middle tier consists of a linker helical domain (LHD) containing twelve helices (LH1-LH12), and forms the scaffold for multiple inter-domain interactions within the subunit. Four LHDs in a channel tetramer encircle a fenestrated open court beneath the cytosolic entrance of the channel. Embedded in lipid, the S1-S6 6 transmembrane (6-TM) domain and the TRP domain constitute the top tier of the channel. Like most classical 6-TM tetrameric cation channels, the S1-S6 of each subunit is separated into an S1-S4 voltage-sensing domain (VSD) and an S5-S6 pore domain linked by the S4-S5 linker helix. The tetramer assembly is domain-swapped, with the VSD of one subunit interacting with the pore domain from a neighboring subunit.

N-terminal cytosolic domains

The N-terminal region of TRPM4 contains NBD, ARD and LHD domains. The 400-residue NBD, hypothesized to be the ATP binding site[16], is an α/β protein with a central β-sheet formed by nine predominantly parallel β-strands (β3-β11) and its overall architecture partially resembles the Rossmann-fold dinucleotide binding proteins (Fig. 2a). Structural homology search using DALI server[29] identified an AMP-binding phosphoribohydrolase named lonely guy (LOG) protein[30,31] that has the highest structural similarity to the NBD of TRPM4 (Extended Data Fig. 7a). Two Ankyrin repeats (AR) constitute the ARD and form a rigid unit with the NBD via extensive inter-domain interactions between the AR1 helices and the NBD (Fig. 2b). The ARD also directly interacts with the NBD of the neighboring subunit, mediating the tetrameric assembly at the bottom tier of TRPM4; the inter-subunit interactions are mainly hydrogen bonds between hydrophilic or charged residues (Fig. 2b). Tetramerization of the NBD and ARD generates a wide-open central hole, which is plugged by the C-terminal coiled-coil helices (Fig. 1b). The middle tier LHD has a similar structural arrangement to the linker helices of NOMPC, a mechanosensitive drosophila TRPN channel[32]. LHD barely contributes to the tetrameric assembly, but it provides the hub for multiple inter-domain interactions within the subunit and likely mediates the coupling between the bottom tier NBD/ARD tetramer assembly and the top tier transmembrane domain (Extended Data Fig. 8).

ATP binding and its inhibition of TRPM4

To confirm ATP binding and define its role in TRPM4 activity, we determined the TRPM4 structure in the presence of ATP at 2.9 Å (Methods), allowing us to identify four bound ATP molecules in the channel tetramer, one per subunit (Fig. 2c). The ATP site is located at the inter-subunit interface between the NBD and ARD (Fig. 2c and d), distinct from the classical

nucleotide binding site in proteins with the Rossmann-fold (Extended Data Fig 7a). The adenine moiety of ATP is positioned in a pocket formed by the loops between β6 and α4 and between α5 and β8 of the NBD, and surrounded by aromatic residues of His160, Trp214, and Phe228 (Fig. 2a and c). The triphosphate group protrudes out into the interface and is surrounded by multiple basic residues (Fig. 2c). The triphosphate group appears to be more flexible as its density is less well defined. Structural comparison of TRPM4 in the ATP-bound versus the apo state reveals no global conformational change as the two structures superimposed extremely well in most part of the protein (Extended Data Fig. 7b). The major conformational change occurs locally near the ATP binding site (Fig. 2d): upon ATP binding, the N-terminal half of the NBD swings away from the ARD of a neighboring subunit in a rigid body motion, resulting in the disruption of the inter-subunit interactions at the tetrameric assembly interface.

Cytosolic ATP has divergent effects on TRPM4 activity: free ATP but not the Mg^{2+}-chelated ATP (ATP-Mg) can inhibit the channel[15], while exposing desensitized TRPM4 to ATP-Mg can alleviate desensitization, thereby increase channel conductance[13,16]. To define the role of ATP binding at NBD, we mutated the three aromatic residues at the ATP binding site to alanine, individually. All mutations resulted in reduced ATP inhibition with the His160Ala mutation having the most profound effect (Fig. 2e and Extended Data Fig. 7c). The His160Ala mutant, however, exhibits the same recovery from steady state desensitization as the wild type channel when exposed to ATP-Mg (Extended Data Fig. 7d), indicating that ATP binding at NBD plays inhibitory role in TRPM4 activity. Therefore the ATP-bound TRPM4 structure represents an ATP-inhibited closed state. The channel recovery from desensitization was suggested to be caused by ATP-Mg activation of a lipid kinase that restores the membrane $PtdInsP_2$ level[13]. Because the ATP specificity in TRPM4 is mainly defined by the adenine moiety of the nucleotide (Fig. 2c), ADP and AMP can also bind and inhibit TRPM4[15]. The basic residues surrounding the ATP site likely stabilize the negatively charged triphosphate group and may prevent the binding of ATP-Mg. The aromatic residues important for ATP binding in TRPM4 are not conserved in TRPM5 (Extended Data Fig. 6), explaining the lack of ATP inhibition in TRPM5[33]. The ATP inhibition in TRPM4 is also distinct from that in TRPM6/7[34,35]. TRPM6/7 is inhibited by Mg-ATP, but not free ATP, and the inhibition likely involves the C-terminal kinase domain that is absent in TRPM4.

With a binding site distant from the ion conduction pore, ATP inhibition is the result of an allosteric gating modulation instead of channel blocking, and the strategic location of the ATP site between the NBD and ARD provides a plausible explanation. Upon channel activation, the cytosolic tetrameric assembly likely undergoes a concerted conformational change, which requires the rearrangement of inter-subunit contact at the assembly interface. We suspect that the interfacial ATP binding causes the NBD and ARD to detach at the assembly interface, which in turn prevents the cytosolic tetramer assembly from undergoing any concerted movement associated with channel activation, and thereby inactivates the channel.

Ion conduction pore and selectivity

The TRPM4 ion conduction pore, consisting of the S5, S6 and pore helix (P), adopts the closed conformation (Fig. 3a and b). The four pore-lining S6 inner helices form a bundle crossing at the cytosolic side with a narrow constriction point of 1 Å radius formed by I1036, preventing ion passage. TRPM4 has an exceptionally long loop between the filter and S6, which forms an extracellular turret and encircles a deep vestibule at the external entrance of the channel. The inner surface of the vestibule is lined with multiple acidic residues, generating a highly negative surface potential (Fig. 3a and c).

TRPM4 has a short but wide selectivity filter consisting of the sequence ^{971}Phe-Gly-Gln (Fig. 3d). The backbone carbonyls of Phe971 and Gly972 along with the Gln973 side chain line the ion conduction pathway with a minimum atom-to-atom diameter of ~7.6 Å between Gly972 carbonyl oxygen atoms, suggesting the passage of hydrated ions during ion conduction. Notably, TRPM4 is monovalent selective and impermeable to divalent Ca^{2+} or Mg^{2+}. We suspect that the selectivity of TRPM4 is partly determined by the hydrated ion radius, of which, group II divalents are larger than group I monovalents[36]. Gln973 plays an essential role in monovalent selectivity of TRPM4[37]; its sidechain forms a hydrogen-bond with the backbone carbonyl of Gly972 from the neighboring subunit and likely stabilizes the filter configuration. Replacing Gln973 with Glu, Asn or Asp all resulted in increased Ca^{2+} permeation (Fig. 3e). In particular, the Gln973Asp mutant has almost equal permeability between Na^{+} and Ca^{2+} (P_{Na}/P_{Ca}~1.6) (Fig. 3e and Extended Data Fig. 9). Within the filter and central cavity, multiple electron density peaks are clearly visible and modeled as water and Na^{+}, the only cation in the sample (Fig. 3d). Most of the distances between the ions and the oxygen atoms from protein or water are in the range of 4–5 Å, too far for direct ion chelation. These oxygen ligands probably stabilize the hydrated monovalent cation by acting as the 2nd hydration shell.

S1-S4 domain and post-S6 TRP domain

The S1-S4 domain of TRPM4 consists of four straight helices tightly packed against each other and adopts a structure similar to that of TRPV1 (Fig. 4 and Extended Data Fig. 10a). Despite the presence of one arginine (Arg901) on S4, this arginine does not contribute to voltage sensing as replacing it with alanine did not change the voltage dependence of TRPM4 in the desensitized state (Extended Data Fig. 10b). Furthermore, the S4 helix runs antiparallel to the S5 helix of a neighboring subunit with extensive hydrophobic interactions and is unlikely to undergo a similar translational movement expected for a voltage-sensing S4[38–40] (Fig. 4a). Therefore, S1-S4 is not the voltage sensor of TRPM4 and likely remains static during channel gating. Near the intercellular membrane surface, the S1-S4 helices and the TRP domain enclose a solvent accessible cavity surrounded by a large number of basic and acidic residues (Fig. 4a).

The post-S6 TRP domain of TRPM4 is longer than the conventionally defined one[2] and consists of two helices, named TRP helix 1 and TRP helix 2 (Fig. 4). TRP helix 1 contains the conserved TRP box and runs immediately after S6 as a curved helix with its apical side coupled to the S4-S5 linker through tight hydrophobic packing (Fig. 4b). The C-terminal end of the TRP helix 1 is positioned right underneath the S1-S4 domain with Glu1064 and

Arg1068 pointing their side chains into the intracellular-facing cavity. Glu1064 was shown to be important for Ca^{2+} activation[41] and we suspect the cavity could potentially house the Ca^{2+} binding site. TRP helix 2 and the loop between the two TRP helices are buried in the lower leaflet of the membrane; the loop also participates in the formation of the cavity with S1-S4 by patching the side opening. The TRP helix 2 is not present in TRPV or TRPA channel structures but was observed in NOMPC[32,42,43].

The S1-S4 and TRP domains form a tightly associated entity directly coupled to the intracellular gate of the pore with S1-S4 connected to S5 through S4-S5 linker and TRP helix 1 directly linked to the pore-lining S6 helix (Fig. 4a). They likely serve as the central gating apparatus of the channel. $PtdInsP_2$ probably modulates TRPM4 activity by binding in the S1-S4 domain similar to that in TRPV1[44]. Although the exact locations for Ca^{2+} and $PtdInsP_2$ binding in TRPM4 remain to be identified, we suspect both ligands bind at the S1-S4/TRP gating apparatus and trigger conformational changes that are coupled to the pore opening via the S4-S5 linker and/or TRP helix 1.

Stretcher helix and coiled coil

The C-terminal domain of TRPM4 contains the coiled coil helix and a long preceding stretcher helix so named for its architectural resemblance to the stretcher of an umbrella. In the channel tetramer, four stretcher helices span from the periphery towards the center and converge on the long four-helix coiled coil that runs vertically through the central hole of the bottom tier tetramer assembly formed by the NBD and ARD (Fig. 5a). Other than the covalent linkage to the stretcher helices, the coiled coil does not appear to make any specific contact with the surrounding NBD/ARD, allowing it to slide within the central hole. The primary contact between the C-terminal stretcher/coiled-coil helices and the rest of the channel is mediated by the middle tier LHD, with a mixture of hydrogen bonds and hydrophobic packing between the N-terminus of the stretcher helix and the LH7-8 (Fig. 5b).

The functional role of the TRPM4 C-terminal domain, if any, remains elusive and warrant further study. The previously proposed modulation sites for phosphorylation, $PtdInsP_2$ binding or calmodulin binding at the C-terminal domain do not appear to be accessible based on the structure[14,16]. However, the structural feature of the C-terminal domain would imply that the coiled coil is capable of undergoing an up-and-down sliding motion, which, in turn, can induce lateral movement through the stretcher helices and propagate to the channel transmembrane pore through the middle tier LHD (Fig. 5c). This could potentially be the structural mechanism of TRPM channel modulation at the C-terminus and may occur in some TRPM chanzymes whose functional enzyme domains are located immediately after the coiled coil.

Summary

In conclusion, the TRPM4 channel structures provide an initial glimpse of the molecular architecture of the TRPM family. $PtdInsP_2$ and Ca^{2+} probably bind at the transmembrane gating apparatus formed by S1-S4 and TRP domains and activate the channel via conformational change at the S4-S5 linker and/or TRP helix 1 (Fig. 5c). ATP binding at the NBD disrupts the bottom tier tetrameric assembly and allosterically inactivates the channel.

The C-terminal coiled-coil could potentially undergo a piston-like motion and modulate the channel gating via the stretcher helix. Several important questions pertaining to TRPM4 gating remain to be addressed, including the structural mechanisms of Ca^{2+} activation, $PtdInsP_2$ potentiation, Ca^{2+} desensitization, and voltage-dependence. Our initial structures, however, provide an essential starting point for elucidating the complex gating mechanisms of TRPM4.

Methods

Protein expression, purification, and nanodisc reconstitution

Mouse TRPM4 (NCBI accession BC096475) containing a C-terminal 10× His tag was cloned into a pEG BacMan vector[45] and heterologously expressed in HEK293F cells (Life Technologies) using the BacMam system (Thermo Fisher Scientific). The baculovirus was generated in Sf9 cells (Life Technologies) following standard protocol and was used to infect HEK293F cells at a ratio of 1: 40 (virus: HEK293F, v:v), supplemented with 10 mM sodium butyrate to boost protein expression.

Cells were cultured in suspension at 37 °C for 48 hours and harvested by centrifugation at 3,000 × g. The cell pellet was re-suspended in buffer A (20 mM Tris pH 8.0, 150 mM NaCl) supplemented with a protease inhibitor cocktail (containing 2 μg/mL each of DNase I, 0.5 μg/mL pepstatin, 2 μg/mL leupeptin and 1 μg/mL aprotinin, and 0.1 mM PMSF) and homogenized by sonication on ice. TRPM4 was extracted with 2% (w:v) n-Dodecyl-β-D-Maltopyranoside (DDM, Anatrace) supplemented with 0.2% (w:v) cholesteryl hemisuccinate (CHS, Sigma Aldrich) by gentle agitation for 2 hours on ice. After extraction, the supernatant was collected following a 40-minute centrifugation at 48,000 × g and incubated with Ni-NTA resin (Qiagen) with gentle agitation, supplemented with 30 mM imidazole. After 4 hours, the resin was collected on a disposable gravity column (Bio-Rad), washed in buffer B (buffer A + 0.1 % DDM + 0.02% CHS) with imidazole at 30 mM and 60 mM for 3 column volumes each. TRPM4 was eluted with 300 mM imidazole, concentrated, and further purified by size exclusion chromatography on a Superose 6 10/300 GL column (GE Heathcare) pre-equilibrated with buffer B.

The protein peak was collected, concentrated to 40 μM and reconstituted into lipid nanodiscs following published protocol[44]. Briefly, TRPM4, MSP1[46] and lipid (POPC: POPG: POPE = 3:1:1) were mixed at a molar ratio of 1:4:30, and incubated on ice for 30 minutes. Detergents were removed by adding Bio-beads SM2 (Bio-Rad) to a concentration of 100 mg/ml followed by gentle agitation. The used bio-beads were replaced with fresh ones every 4 hours for two times. After detergent removal, the sample was loaded onto a Superose 6 10/300 GL column pre-equilibrated with buffer A and the elution peak corresponding to the reconstituted TRPM4 was collected for cryo-electron microscopy analysis (Extended Data Fig. 2).

EM data acquisition

The cryo-EM grids were prepared by applying 3 μl of TRPM4 in nanodiscs (1.8 mg/ml) to a glow-discharged Quantifoil R1.2/1.3 200-mesh copper holey carbon grid (Quantifoil, Micro

Tools GmbH, Germany) and blotted for 4.0 seconds under 100% humidity at 4 °C before being plunged into liquid ethane using a Mark IV Vitrobot (FEI). Micrographs were acquired on a Titan Krios microscope (FEI) operated at 300 kV with a K2 Summit direct electron detector (Gatan), using a slit width of 20 eV on a GIF-Quantum energy filter. EPU software (FEI) was used for automated data collection following standard FEI procedure. A calibrated magnification of 46,730× was used for imaging, yielding a pixel size of 1.07 Å on images. The defocus range was set from -1.5 μm to -3 μm. Each micrograph was dose-fractionated to 30 frames under a dose rate of 4 e^-/pixel/s, with a total exposure time of 15 s, resulting in a total dose of about 50 $e^-/Å^2$. The ATP-bound TRPM4 sample was prepared by adding 5 mM Na_2. ATP and 2 mM $CaCl_2$ into the TRPM4 in nanodiscs, resulting in a sample with 3 mM free ATP, 0.1 mM free Ca^{2+}, and about 2 mM Ca-ATP (http://maxchelator.stanford.edu). Only free ATP can bind and inhibit TRPM4 as demonstrated in previous functional study as well as this structural study. Despite the presence of 0.1 mM Ca^{2+} in the sample, we did not observe bound Ca^{2+} in the ATP-bound TRPM4 structure. This could be because of the low apparent affinity of Ca^{2+} in the absence of $PtdInsP_2$, resulting in a low Ca^{2+} occupancy at 0.1 mM concentration. Further study is required to capture the Ca^{2+}-bound state.

Image processing

For the TRPM4 apo form dataset, motion correction was performed using the MotionCorr2 program[47], and the CTF parameters of the micrographs were estimated using the GCTF program[48]. All other steps of image processing were performed using RELION 2.0[49]. Initially, about 1,000 particles were manually picked from a few micrographs. Class averages representing projections of TRPM4 in different orientations were selected from the 2D classification of the manually picked particles, and used as templates for automated particle picking from the full data set of 2,876 micrographs. The extracted particles were binned 3 times and subjected to two rounds of 2D classification, and a total of 437,984 particles were finally selected for 3D classification using the initial model generated by RELION as the reference. Four of the 3D classes showed good secondary structural features and their particles were selected, combined and re-extracted into the original pixel size of 1.07 Å. After 3D refinement with *C4* symmetry imposed and particle polishing, the resulting 3D reconstructions from 140,259 particles yielded an EM-map with a resolution of 3.1 Å. The C-terminal part of the coiled coil domain showed poor density, indicating a local structural heterogeneity. Therefore, we performed a focused 3D classification with density subtraction in order to improve the density of the coiled coil domain[50]. In this approach, only the density corresponding to the coiled coil domain was kept in each particle image by subtracting the density for all other parts including the nanodisc from the original particles. In the subsequent 3D classification on the modified particles, a soft mask was applied around the coiled coil domain and all the particle orientations were fixed at the value determined in the initial 3D refinement that generated the 3.1 Å map. After this round of classification, one class (11,545 particles) showed a better density in the coiled coil domain. The corresponding particles before density subtraction from this class were selected and 3D refined, yielding an EM map of 3.5 Å for the entire channel in which most part of coiled coil domain can be modeled. The data for the ATP bound TRPM4 was processed following the same procedure. Briefly, 564,549 particles were auto-picked from 2,752 micrographs, and

after 2D and 3D classification, 196,618 particles were selected for the final 3D reconstruction and refinement, resulting in an ATP bound TRPM4 structure with an overall resolution of 2.9 Å after particle polishing. The focused 3D classification at the coiled coil domain was also performed on the ATP bound data. All resolutions were estimated by applying a soft mask around the protein density and the gold-standard Fourier shell correlation (FSC) = 0.143 criterion. ResMap[51] was used to calculate the local resolution map.

Model building, refinement, and validation

De novo atomic model building was conducted in Coot[52]. Amino acid assignment was achieved based on the clearly defined density for bulky residues (Phe, Trp, Tyr, and Arg). Models were refined against summed maps using phenix.real_space_refine[53], with secondary structure restraints applied. The model was validated using previously described methods to avoid overfitting[54,55]. The initial 3.1 Å EM density map of apo TRPM4 allowed us to construct a model containing residues 12-24, 68-317, 331-386, 396-484, 501-511, 556-712, 765-830, 848-1090, and 1112-1162. The 3.5 Å EM map, derived from the focused 3D classification at the coiled coil region, further extended the model at the C-terminus by 31 residues (from Gly1162 to Ser1193), which were modeled as poly-alanines due to the pore side chain density. Therefore, in all structure representations, the C-terminal coiled coil was extended to Ser1193. The final model for the ATP-bound TRPM4 contained residues 12-24, 68-317, 331-484, 501-519, 557-712, 765-830, 848-1090, and 1112-1193. The statistics for the models' geometries was generated using MolProbity[56]. Pore radii were calculated using the HOLE program[57]. All the figures were prepared in PyMol[58] or Chimera[59].

Electrophysiology

The *trpm4* cDNA was cloned into SalI/SacII sites of the pEGFP-N1 vector (Clontech). All single-site mutants were generated using Quikchange Site-Directed Mutagenesis Kit (Agilent) and confirmed by DNA sequencing. 1-2 μg of the plasmid was transfected into HEK293 cells that were grown as a mono-layer in 35-mm tissue culture dishes (to ~70% confluence) using Lipofectamine 2000 (Life Technology). 24-48 h after transfection, cells were dissociated by trypsin treatment and kept in complete serum-containing medium and re-plated onto 35-mm tissue culture dishes and incubated in a tissue culture incubator until recording. Patch clamp recording in inside-out configuration was employed to measure both single channel and macroscopic currents of TRPM4 or its mutants overexpressed in HEK293 cells. The standard bath solution (cytosolic side) contained (in mM): 145 Cesium methanesulfonate (Cs-MS), 5 NaCl, 1 $MgCl_2$, 0.3 $CaCl_2$, 10 HEPES buffered with Tris, pH=7.4. For calcium free condition, 0.5 mM EGTA was added to the bath solution without $CaCl_2$. The pipette solution (extracellular side) contained (in mM): 150 Na-MS, 1 $MgCl_2$, 5 $CaCl_2$, 10 HEPES buffered with Tris, pH=7.4. The data was acquired using an AxoPatch 200B amplifier (Molecular Devices) and a low-pass analogue filter set to 1 kHz. The current signal was sampled at a rate of 20 kHz using a Digidata 1322A digitizer (Molecular Devices) and further analyzed with pClamp 9 software (Molecular Devices). Patch pipettes were pulled from borosilicate glass (Harvard Apparatus) and heat polished to a resistance of 3-5 MΩ. After the patch pipette attached to the cell membrane, a giga seal (> 10 GΩ) was

formed by gentle suction. The inside out configuration was formed by pulling the pipette away from the cell and the pipette tip was exposed to air for a short time in some cases. The holding potential was set to 0 mV. The current and voltage relationship (I-V curve) was obtained using voltage pulses ramp from -100 to +100 mV over an 800-ms duration. Sample traces for single channel recording or the I-V curves of macroscopic currents shown in each figure were obtained from recordings on the same patch. The lipid ligands used in this study are phosphatidylinositol-4,5-bisphosphate diC8 (PtdIns(4,5)P_2 diC8, Echelon). All data points shown in Fig. 2e, Extended Data Fig. 1e and Extended Data Fig. 10b are mean ± SEM of five measurements from different patches (n =5 independent biological replicates).

The chelation of ATP with Mg^{2+} and Ca^{2+} were taken into account in the measurement of cytosolic ATP inhibition of TRPM4. Specific amounts of $CaCl_2$, $MgCl_2$, and Na_2. ATP were prepared according to MAXCHELATOR (http://maxchelator.stanford.edu) to achieve the targeted concentrations of free ATP (0.1, 0.3, 1.6, 8.5, 42.0 or 160.0 μM) in the bath solutions with the presence of a constant free Ca^{2+} of 0.3 mM.

The voltage dependence of TRPM4 was measured after the channel reached the Ca-desensitized steady state in the presence of 0.3 mM cytosolic Ca^{2+} without PI(4,5)P_2. To generate G/G_{max} versus V curves ($G=I/V$), the membrane was stepped from the holding potential (0 mV) to various testing potentials (−100 mV to +100 mV) for 1s and then step to -100 mV. The peak tail currents were used to plot G-V curves. G_{max} was obtained from the peak tail current at 120 mV testing potential. $V_{1/2}$ and Z values were obtained from fitting the data to the Boltzmann equation, where $V_{1/2}$ is the voltage at which the channels have reached half of their maximum fraction open and Z is the apparent valence of voltage dependence.

In the measurement of monovalent cation selectivity, the bath solution (in mM) contained 150 X-MS (where X=Li, Na, K, or Cs), 1 $MgCl_2$, 0.3 $CaCl_2$, 10 HEPES buffered with Tris, pH 7.4. To measure calcium selectivity, the pipette solution was changed to (in mM) 95 Ca-MS_2, 5 $CaCl_2$, 10 HEPES buffered with Tris, pH 7.4, and the bath solution contained 150 Na-MS, 1 $MgCl_2$, 0.3 $CaCl_2$, 10 HEPES buffered with Tris, pH=7.4. The ion permeability ratios were calculated with the following equations:

$$P_{Na}/P_x = [Na]_{pipette}\exp\left(V_{rev}F/RT\right)/[X]_{bath}, \ (X = \text{Li, Na, K or Cs})$$

$$P_{Na}/P_{Ca} = 4[Ca]_{pipette}/\left\{[Na]_{bath}\exp\left(V_{rev}F/RT\right)(1+\exp\left(V_{rev}F/RT\right)\right\}$$

where V_{rev} is the reverse potential of the I-V curves, F is Faraday's constant, R is the gas constant, and T is the absolute temperature.

In the analysis of Ca^{2+} activation of TRPM4, the normalized activation current (I/I_{max}) at 100 mV as a function of free [Ca^{2+}] was fitted with the Hill equation:

$$I/I_{max} = 1 / [1 + ([Ca^{2+}]/EC_{50})^{-n}]$$

where I_{max} is the current at 30 μM $[Ca^{2+}]$ in the presence of 10 μM PtdIns(4,5)P_2 or at 3 mM $[Ca^{2+}]$ in the absence of PtdIns(4,5)P_2, EC_{50} is the half maximal effective concentration and n is the Hill coefficient.

In the analysis of ATP inhibition of TRPM4, the fraction of unblocked current (I/I_{max}) at 100 mV as a function of free [ATP] was fitted with the Hill equation:

$$I/I_{max} = 1 / [1 + ([ATP]/IC_{50})^{n}]$$

where I_{max} is the current at 0 mM ATP, IC_{50} is the inhibition constant which is equal to the concentration of the inhibitor required to achieve 50% reduction in current, and n is the Hill coefficient.

Data availability

The cryo-EM density maps of the mouse TRPM4 in nanodisc have been deposited in the Electron Microscopy Data Bank under accession numbers EMD-7081 for apo state with shorter coiled (overall), EMD-7082 for apo state with longer coiled coil (after focused 3D classification), EMD-7083 for ATP-bound state with shorter coiled (overall) and EMD-7085 for ATP-bound state with longer coiled coil (after focused 3D classification). Atomic coordinates have been deposited in the Protein Data Bank under accession numbers 6BCJ for apo state with shorter coiled coil, 6BCL for apo state with longer coiled coil, 6BCO for ATP-bound state with shorter coiled coil, and 6BCQ for ATP-bound state with longer coiled coil. Source data for Fig. 2e, Extended Data Fig. 1e and Extended Data Fig. 10b are available in Supplementary Information.

Extended Data

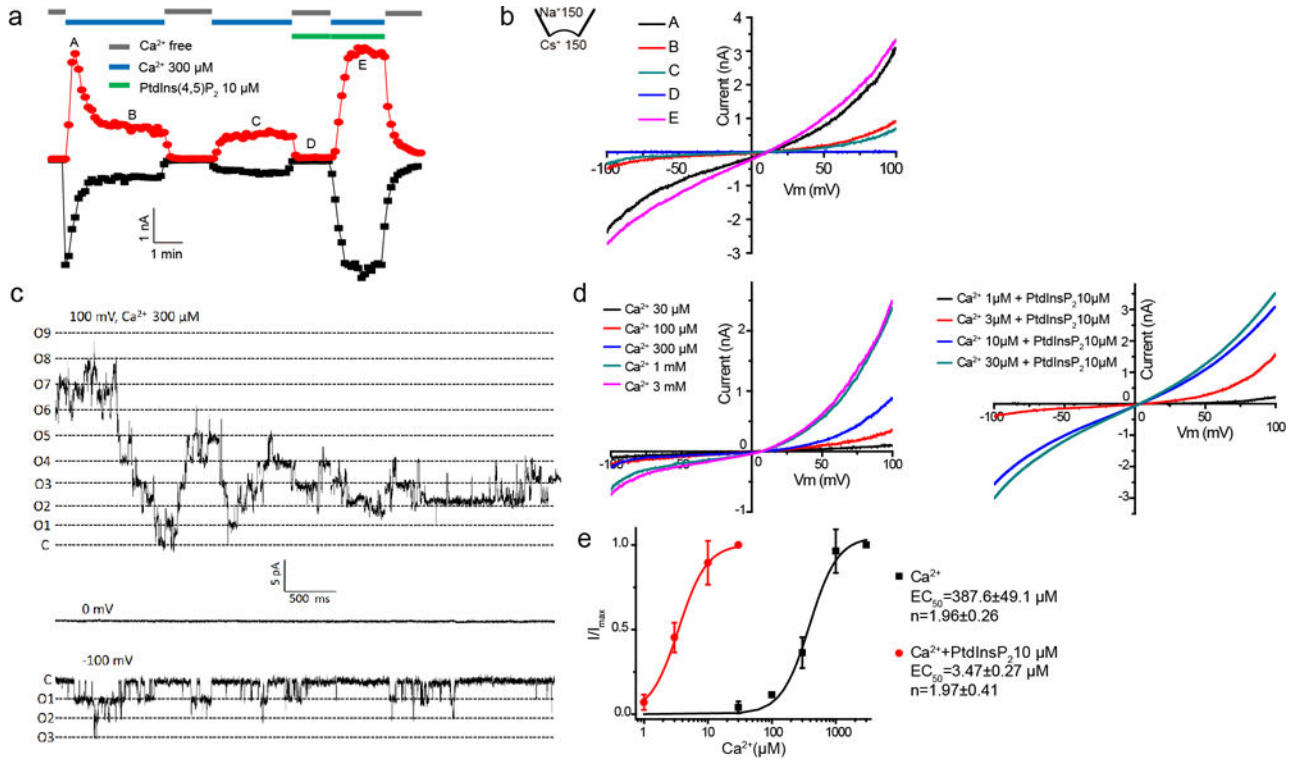

Extended Data Figure 1. Gating properties of mouse TRPM4 overexpressed in HEK293 cells

a, Macroscopic currents of TRPM4 at ±100 mV in an inside-out patch in the presence and absence of various ligands in the bath (cytosolic). **b**, I-V curves of TRPM4 at the time points indicated in **a**. **c**, Sample traces of single channel recordings of TRPM4 in the Ca^{2+}-desensitized state (with 300 μM Ca^{2+}) at 100 mV (top), 0 mV (middle) and −100 mV (bottom), revealing the voltage-dependent single channel open probability. **d**, Sample I-V curves of TRPM4 recorded with various cytosolic (bath solution) Ca^{2+} concentrations in the presence and absence of 10 μM PtdIns(4,5)P_2. **e**, Concentration dependent Ca^{2+}-activation of TRPM4 channels in the presence and absence of PtdIns(4,5)P_2. I/I_{max} were measured at 100 mV from I-V curves shown in **d**. Data were reported as mean ± SEM of five independent biological replicates. Source data are available in Supplementary Information. Curves are least square fits to Hill equation and the result indicates that Ca^{2+} has much lower apparent affinity for desensitized TRPM4. All electrophysiological recordings were repeated at least five times using different patches.

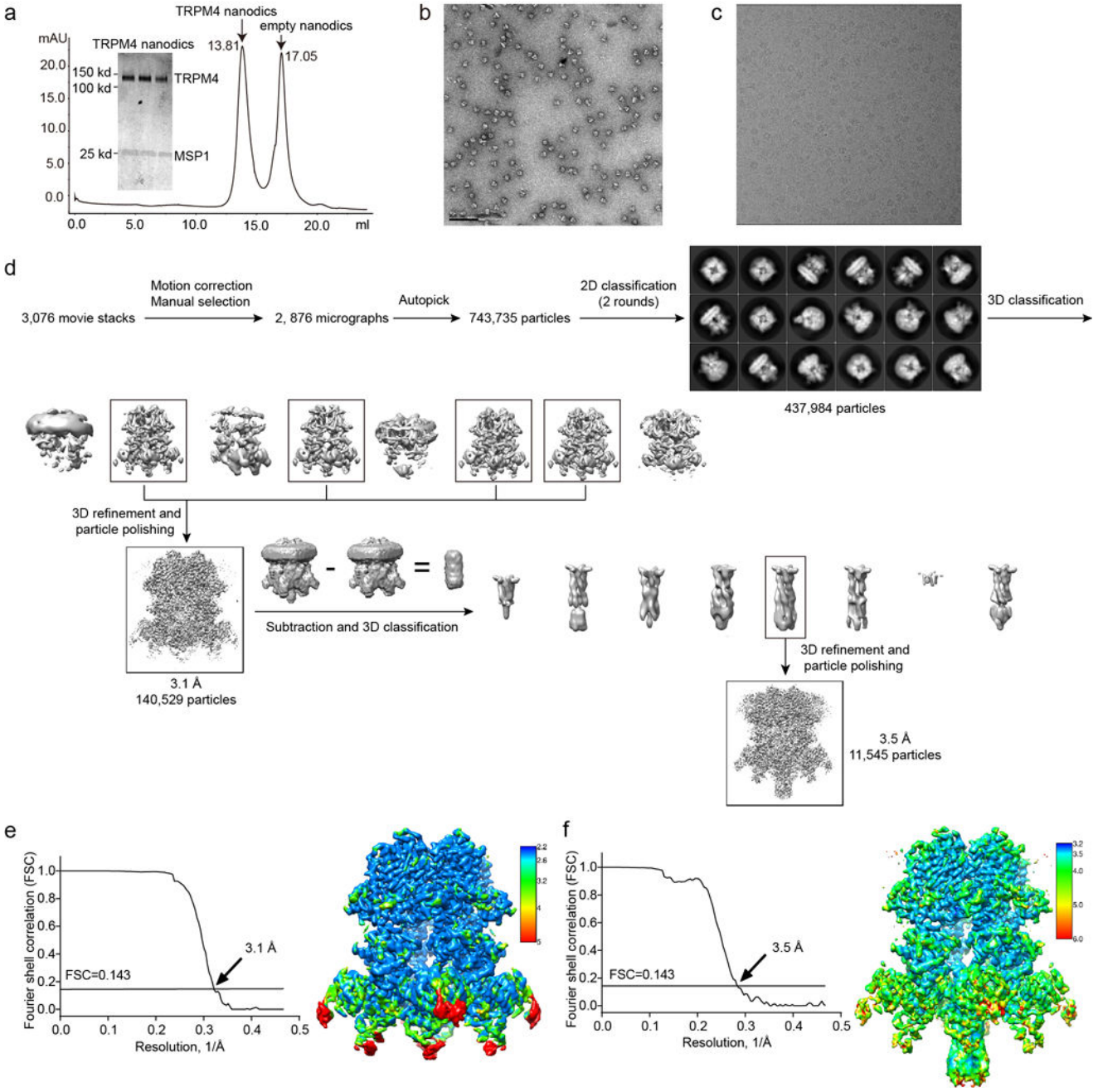

Extended Data Figure 2. Structure determination of apo TRPM4

a, purification of TRPM4 reconstituted in nanodiscs by size exclusion chromatography. **b**, Negatively stained micrograph of TRPM4 in nanodiscs. **c**, Representative cryo-EM micrograph of TRPM4 in nanodiscs. **d**, Flowchart of image processing for apo TRPM4 particles. **e**, Gold-standard FSC curve of the final 3D reconstruction of the apo TRPM4 and the density map colored by local resolution. **f**, Gold-standard FSC curve of particles from the focused 3D classification at the coiled-coil region and the density map colored by local resolution.

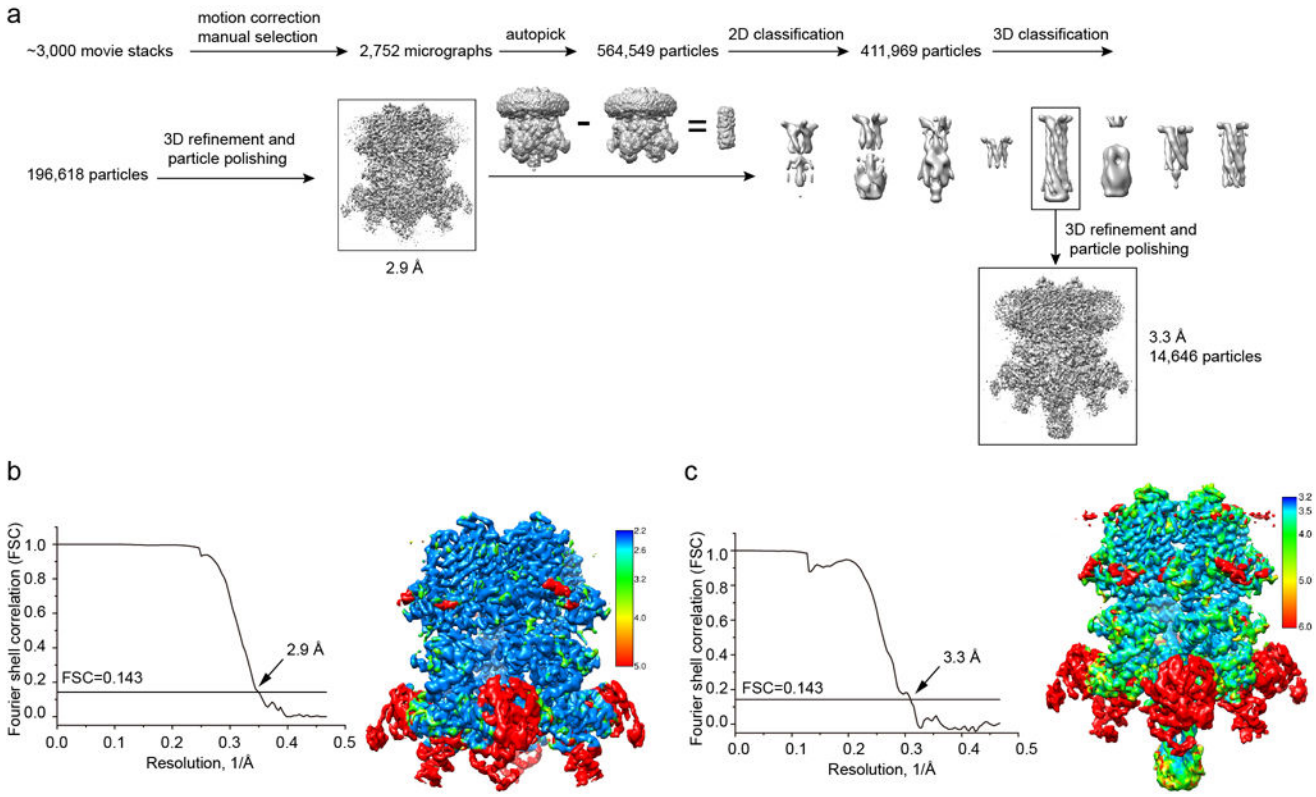

Extended Data Figure 3. Structure determination of ATP-bound TRPM4

a, Flowchart of image processing for ATP-bound TRPM4 particles. **b**, Gold-standard FSC curve of the final 3D reconstruction of the TRPM4-ATP complex and the density map colored by local resolution. **c**, Gold-standard FSC curve of particles from the focused 3D classification at the coiled-coil region of TRPM4-ATP complex and the density map colored by local resolution.

a

	Apo TRPM4	ATP bound TRPM4
Data collection and processing		
Magnification	46730	46730
Voltage (kV)	300	300
Electron exposure (e–/Å^2)	~50	~50
Defocus range (μm)	-1.5 to -3.0	-1.5 to -3.0
Pixel size (Å)	1.07	1.07
Symmetry imposed	*C4*	*C4*
Initial particle images (no.)	743,375	564,549
Final particle images (no.)	140,259	196,618
Map resolution (Å)	3.1	2.9
FSC threshold		
Refinement		
Initial model used (PDB code)	*de novo*	*de novo*
Model resolution (Å)	3.1	2.9
FSC threshold		
Map sharpening *B* factor (Å^2)	-120.58	-91.16
Model composition		
Non-hydrogen atoms	29876	30440
Protein residues	29864	30316
Ligands	12	124
B factors (Å^2)		
Protein	75.40	43.44
Ligand	42.01	54.61
R.m.s. deviations		
Bond lengths (Å)	0.009	0.007
Bond angles (°)	1.229	1.193
Validation		
MolProbity score	1.45	1.56
Clashscore	2.66	3.78
Poor rotamers (%)	0.38	0.37
Ramachandran plot		
Favored (%)	94.14	94.15
Allowed (%)	5.86	5.85
Disallowed (%)	0	0

b

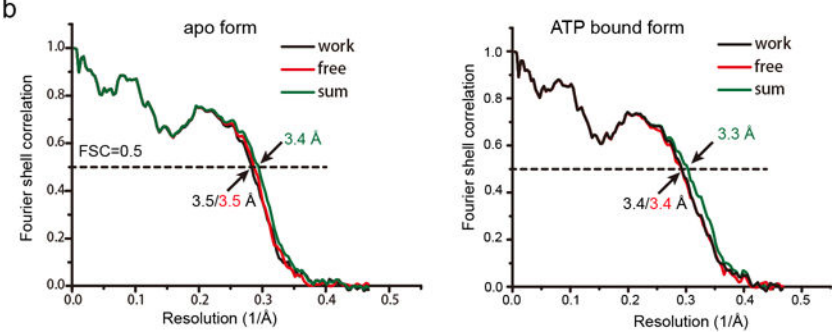

Extended Data Figure 4. Data collection, structure refinement and model validation

a, Data collection and model refinement statistics. **b**, FSC curves for cross-validation between the maps and the models. Curves for model vs. summed map in green (sum), for model vs. half map in black (work), and for model vs. half map not used for refinement in red (free).

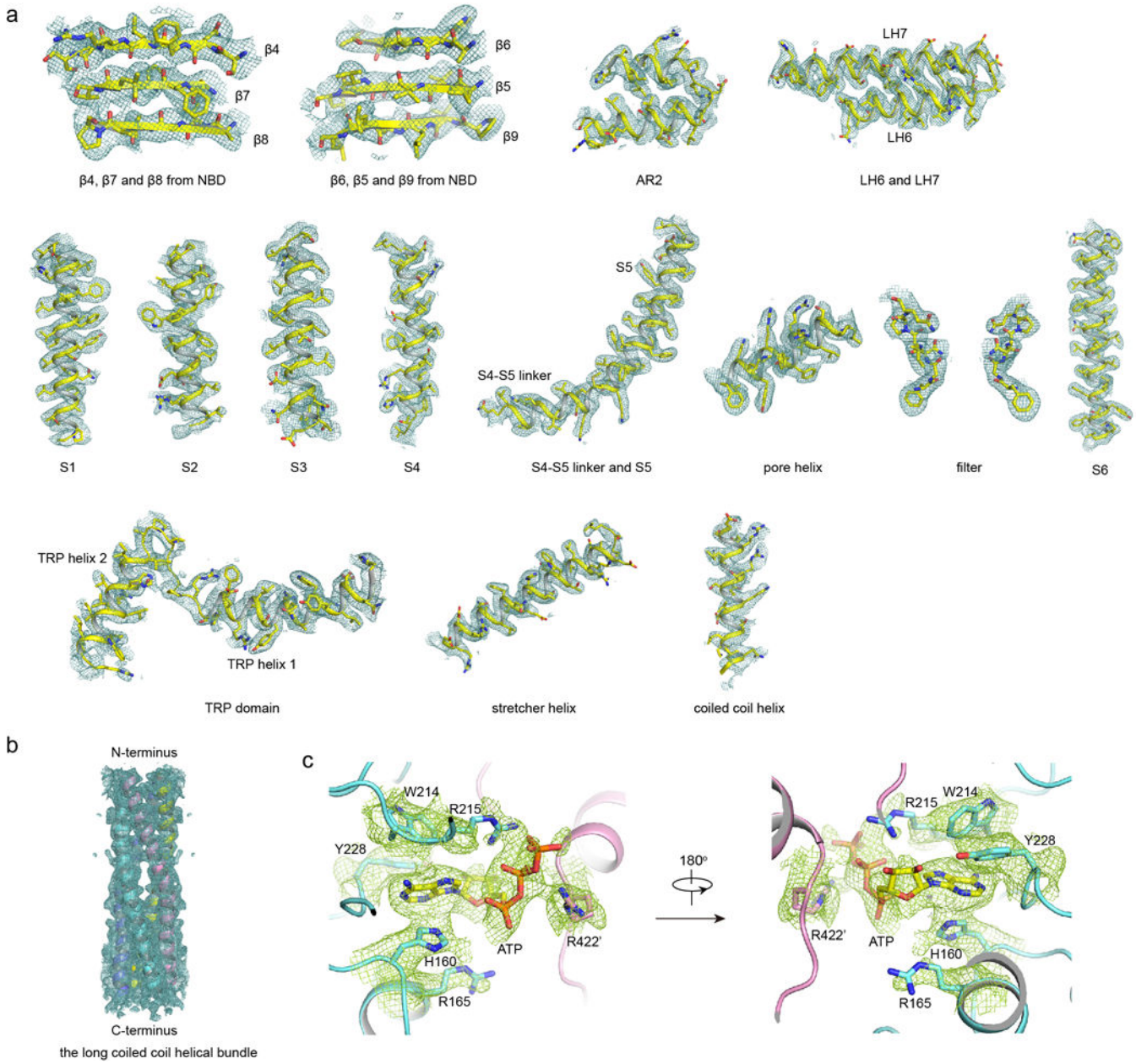

Extended Data Figure 5. Sample EM density maps of TRPM4

a, Sample maps at various regions of apo TRPM4. The maps are low-pass filtered to 3.1 Å and sharpened with a temperature factor of −120 $Å^2$. **b**, EM density of coiled coil region in the apo TRPM4 after focused 3D classification. The map is low-pass filtered to 3.5 Å and sharpened with a temperature factor of −91 $Å^2$. **c**, EM density of ATP and its surrounding residues in the ATP-bound TRPM4. The map is low-pass filtered to 2.9 Å and sharpened with a temperature factor of −91 $Å^2$.

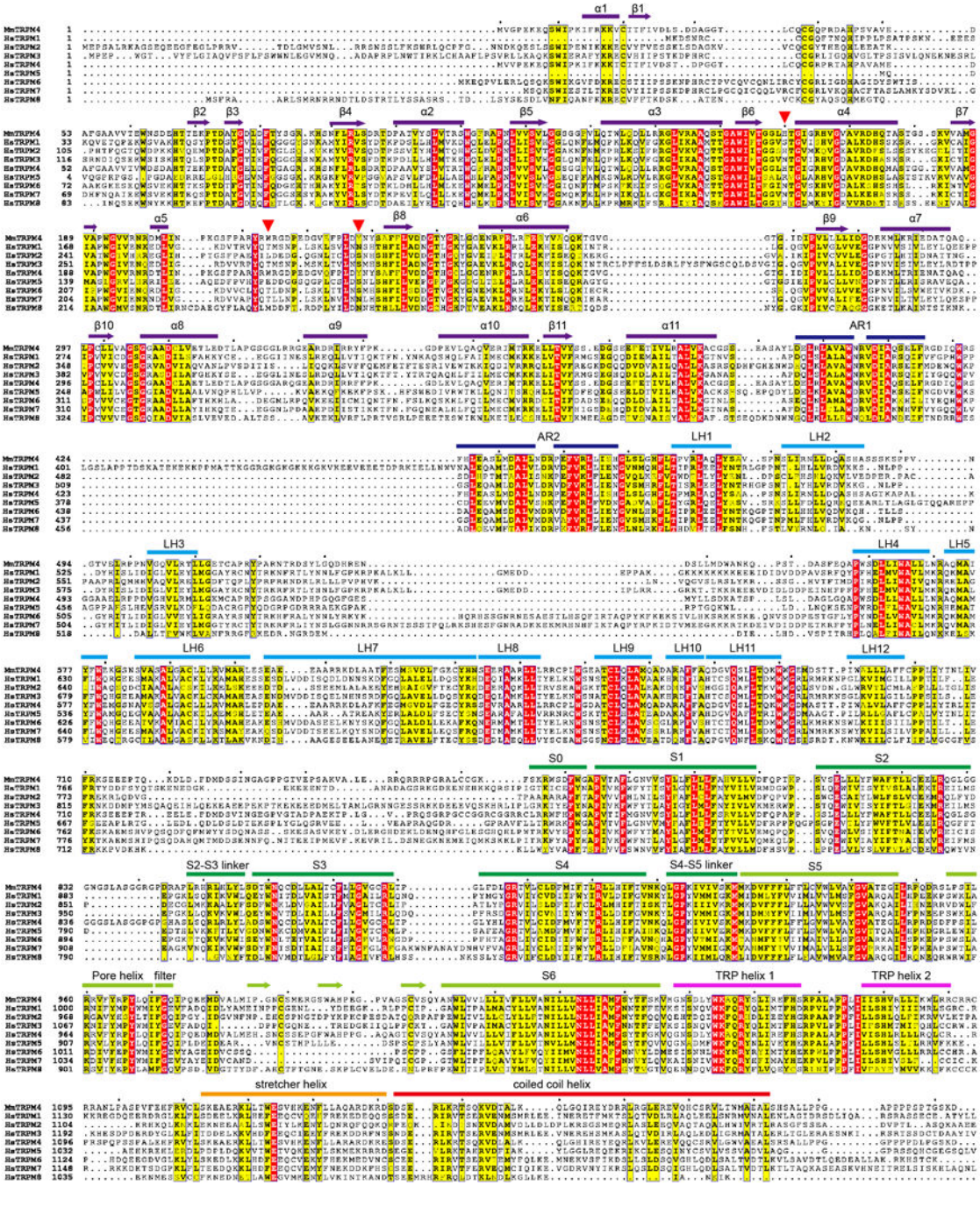

Extended Data Figure 6. Sequence alignment of mouse TRPM4 (MmTRPM4) and human TRPM (HsTRPM1-8) channels

Secondary structure assignments are based on the mouse TRPM4 structure. Only the sequences up to the end of the coiled coil domain are included in the alignment. Red triangles mark the key residues for ATP binding.

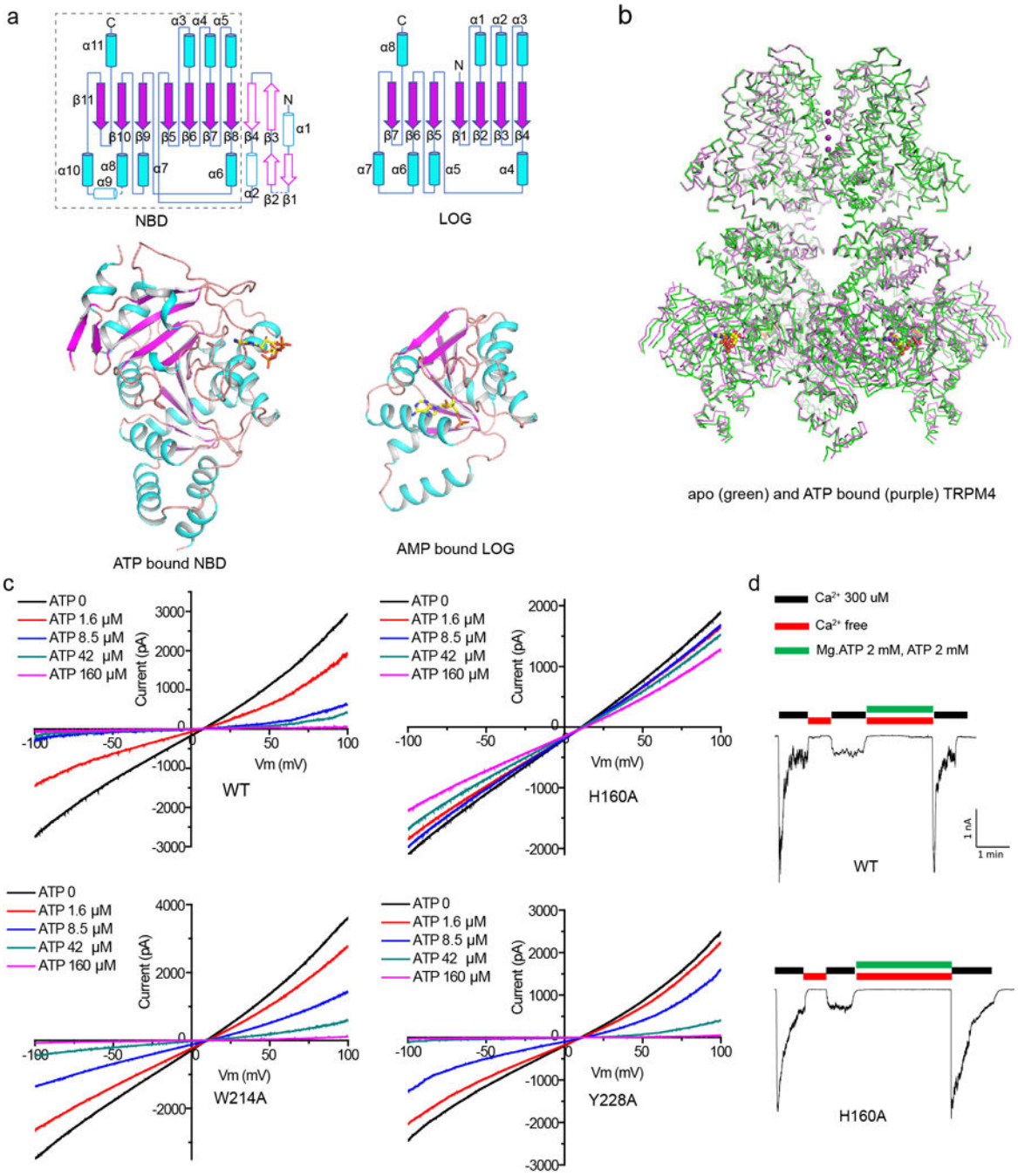

Extended Data Figure 7. NBD structure and ATP inhibition

a, Structural comparison between the NBD of ATP-bound TRPM4 and AMP-bound LOG protein (PDB code 3SBX). The NBD region in the dotted box shares a similar fold to that of LOG protein. The ATP binding site in TRPM4 NBD is distinct from AMP in LOG. **b**, Superposition of TRPM4 structures in the apo (green) and ATP-bound (purple) states. The top two tiers are virtually identical in both states. Major conformational change occurs at the NBD. **c**. Sample I-V curves of TRPM4 and its mutants at various concentrations of cytosolic free ATP. Channels were activated by 300 μM Ca^{2+} and 10 μM PtdIns(4,5)P_2 in the bath

solution. Normalized currents (I/I_{max}) at 100 mV were used to generate the inhibition curves shown in Fig. 2e. I_{max} is the current at 100 mV without ATP. **d**, Recovery of wild-type TRPM4 and H160A mutant activities from Ca^{2+}-desensitization by cytosolic ATP-Mg. Currents were recorded at −100 mV. Note that ATP was washed out before Ca^{2+} activation to avoid ATP inhibition. All electrophysiological recordings were repeated at least five times using different patches.

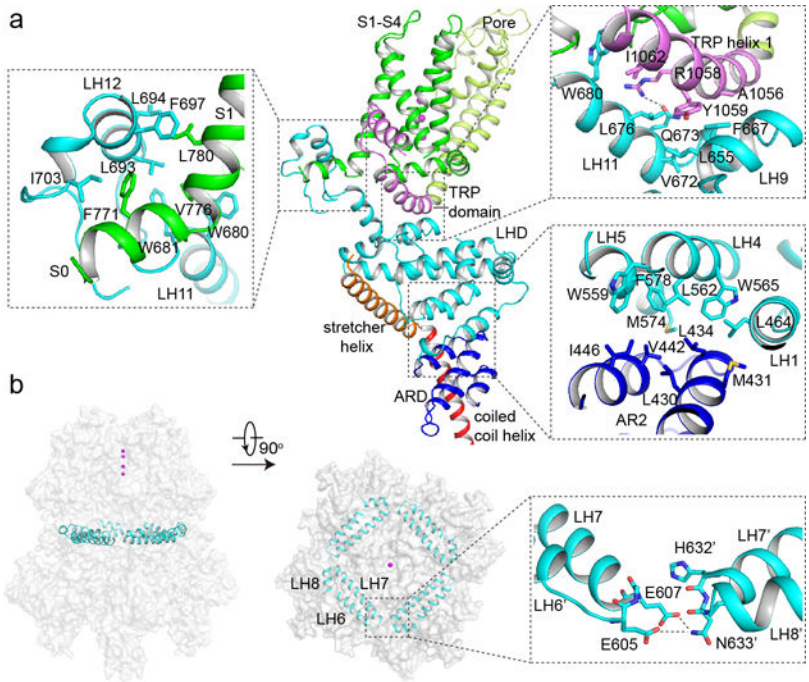

Extended Data Figure 8. Middle-tier linker helical domain mediates inter-domain interactions within the subunit

a, Structure of LHD (cyan) and its interactions with ARD (lower right inset), TRP domain (upper right inset) and S1 helix (left inset). Between the middle and bottom tiers, the linker helices of LH1, 4 and 5 stack atop AR2 and form extensive hydrophobic interactions (lower right inset). The C-terminal part of the LHD mediates direct contacts with the top tier transmembrane domain: the U-shaped LH9-11 grip the bottom side of the TRP helix 1 (upper right inset); LH12 and the loops on its two ends clamp around the S0 and N-terminus of S1 (left inset). **b**, Four linker domains encircle a wide open, fenestrated court at the center of the channel. LH 6-8 helices from each subunit frame the open central court and form head-to-tail packing with their neighboring counterparts in a channel tetramer, providing the only inter-subunit contact at the middle tier.

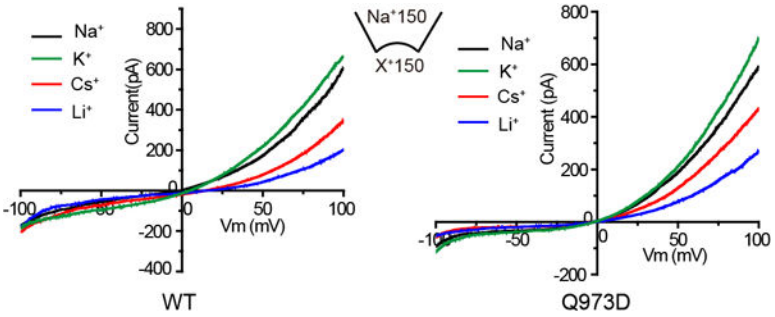

Extended Data Figure 9. Q973D mutant remains non-selective among monovalent cations similar to the wild-type TRPM4 channel

Shown are sample I-V curves recorded in bi-ionic conditions with 150 mM Na^+ in pipette and 150 mM X^+ (X=Li, Na, K or Cs) in bath. Currents were recorded when channels reached desensitized steady state after activation with 300 μM cytosolic (bath) Ca^{2+}. All recordings were repeated at least five times using different patches.

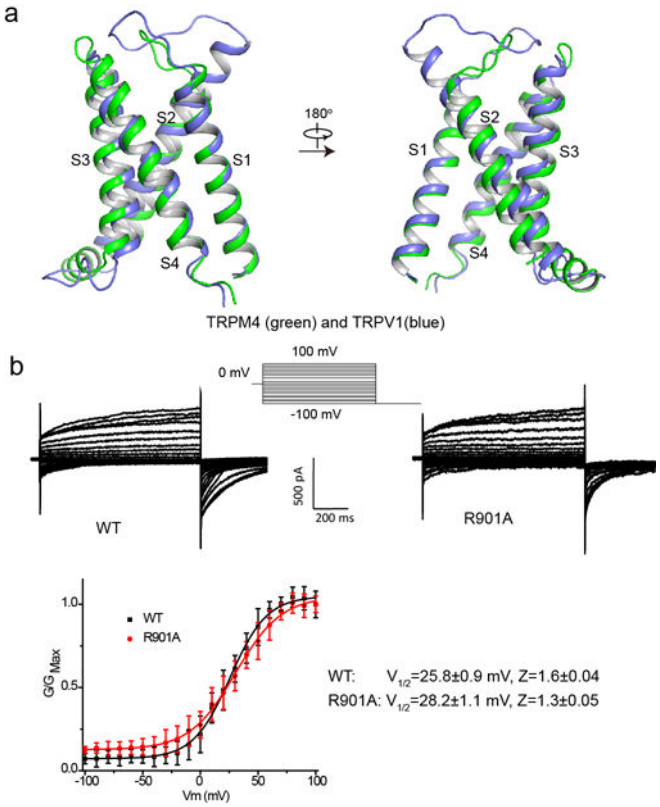

Extended Data Figure 10. S1-S4 domain of TRPM4

a, Structural comparison of S1-S4 domain between TRPM4 (green) and TRPV1 (blue, PDB code 5IRX). **b**, Voltage dependence of wild-type TRPM4 and R901A mutant at Ca^{2+}-desensitized state. The membrane was stepped from the holding potential (0 mV) to various testing potentials (−100 mV to +100 mV) for one second and then step to −100 mV. The peak tail currents were used to plot the G-V curves. Data were reported as mean ± SEM from five independent patches (biological replicates). Source data are available in

Supplementary Information. $V_{1/2}$ and Z values were obtained from fits of the data to the Boltzmann equation.

Supplementary Material

Refer to Web version on PubMed Central for supplementary material.

Acknowledgments

We thank N. Nguyen for manuscript preparation, Dr. J Marc Simard at University of Maryland School of Medicine and Dr. Joseph Bryan at Pacific Northwest Research Institute for providing the TRPM4 clones. Single particle cryo-EM data were collected at the UT Southwestern Medical Center (UTSW) Cryo-Electron Microscopy Facility. We thank D. Nicastro and Z. Chen for support in facility access and data acquisition. Negatively stained sample screening was performed at UTSW Electron Microscopy core. This work was supported in part by the Howard Hughes Medical Institute (Y.J.) and by grants from the National Institute of Health (GM079179 to Y. J.) and the Welch Foundation (Grant I-1578 to Y. J.). X.B. is supported by the Cancer Prevention and Research Initiative of Texas and Virginia Murchison Linthicum Scholar in Medical Research fund.

References

1. Fleig A, Penner R. The TRPM ion channel subfamily: molecular, biophysical and functional features. Trends in pharmacological sciences. 2004; 25:633–639. [PubMed: 15530641]
2. Ramsey IS, Delling M, Clapham DE. An introduction to TRP channels. Annual review of physiology. 2006; 68:619–647.
3. Venkatachalam K, Montell C. TRP channels. Annual review of biochemistry. 2007; 76:387–417.
4. Nadler MJ, et al. LTRPC7 is a Mg.ATP-regulated divalent cation channel required for cell viability. Nature. 2001; 411:590–595. [PubMed: 11385574]
5. Perraud AL, et al. ADP-ribose gating of the calcium-permeable LTRPC2 channel revealed by Nudix motif homology. Nature. 2001; 411:595–599. [PubMed: 11385575]
6. Runnels LW, Yue L, Clapham DE. TRP-PLIK, a bifunctional protein with kinase and ion channel activities. Science. 2001; 291:1043–1047. [PubMed: 11161216]
7. Guinamard R, Demion M, Launay P. Physiological roles of the TRPM4 channel extracted from background currents. Physiology. 2010; 25:155–164. [PubMed: 20551229]
8. Colquhoun D, Neher E, Reuter H, Stevens CF. Inward current channels activated by intracellular Ca in cultured cardiac cells. Nature. 1981; 294:752–754. [PubMed: 6275271]
9. Launay P, et al. TRPM4 is a Ca2+-activated nonselective cation channel mediating cell membrane depolarization. Cell. 2002; 109:397–407. [PubMed: 12015988]
10. Nilius B, et al. Voltage dependence of the Ca2+-activated cation channel TRPM4. The Journal of biological chemistry. 2003; 278:30813–30820. [PubMed: 12799367]
11. Perez CA, et al. A transient receptor potential channel expressed in taste receptor cells. Nature neuroscience. 2002; 5:1169–1176. [PubMed: 12368808]
12. Islam MS. Transient Receptor Potential Channels. Springer Netherlands. 2011:147–171.
13. Zhang Z, Okawa H, Wang Y, Liman ER. Phosphatidylinositol 4,5-bisphosphate rescues TRPM4 channels from desensitization. The Journal of biological chemistry. 2005; 280:39185–39192. [PubMed: 16186107]
14. Nilius B, et al. The Ca2+-activated cation channel TRPM4 is regulated by phosphatidylinositol 4,5-biphosphate. The EMBO journal. 2006; 25:467–478. [PubMed: 16424899]
15. Nilius B, Prenen J, Voets T, Droogmans G. Intracellular nucleotides and polyamines inhibit the Ca2+-activated cation channel TRPM4b. Pflugers Archiv: European journal of physiology. 2004; 448:70–75. [PubMed: 14758478]
16. Nilius B, et al. Regulation of the Ca2+ sensitivity of the nonselective cation channel TRPM4. The Journal of biological chemistry. 2005; 280:6423–6433. [PubMed: 15590641]

17. Earley S, Waldron BJ, Brayden JE. Critical role for transient receptor potential channel TRPM4 in myogenic constriction of cerebral arteries. Circulation research. 2004; 95:922–929. [PubMed: 15472118]
18. Earley S, Straub SV, Brayden JE. Protein kinase C regulates vascular myogenic tone through activation of TRPM4. American journal of physiology. Heart and circulatory physiology. 2007; 292:H2613–2622. [PubMed: 17293488]
19. Del Negro CA, et al. Sodium and calcium current-mediated pacemaker neurons and respiratory rhythm generation. The Journal of neuroscience : the official journal of the Society for Neuroscience. 2005; 25:446–453. [PubMed: 15647488]
20. Mironov SL. Metabotropic glutamate receptors activate dendritic calcium waves and TRPM channels which drive rhythmic respiratory patterns in mice. The Journal of physiology. 2008; 586:2277–2291. [PubMed: 18308826]
21. Cheng H, et al. TRPM4 controls insulin secretion in pancreatic beta-cells. Cell calcium. 2007; 41:51–61. [PubMed: 16806463]
22. Launay P, et al. TRPM4 regulates calcium oscillations after T cell activation. Science. 2004; 306:1374–1377. [PubMed: 15550671]
23. Kruse M, et al. Impaired endocytosis of the ion channel TRPM4 is associated with human progressive familial heart block type I. The Journal of clinical investigation. 2009; 119:2737–2744. [PubMed: 19726882]
24. Liu H, et al. Gain-of-function mutations in TRPM4 cause autosomal dominant isolated cardiac conduction disease. Circulation. Cardiovascular genetics. 2010; 3:374–385. [PubMed: 20562447]
25. Stallmeyer B, et al. Mutational spectrum in the Ca(2+)–activated cation channel gene TRPM4 in patients with cardiac conductance disturbances. Human mutation. 2012; 33:109–117. [PubMed: 21887725]
26. Liu H, et al. Molecular genetics and functional anomalies in a series of 248 Brugada cases with 11 mutations in the TRPM4 channel. PloS one. 2013; 8:e54131. [PubMed: 23382873]
27. Hof T, et al. TRPM4 non-selective cation channel variants in long QT syndrome. BMC medical genetics. 2017; 18:31. [PubMed: 28315637]
28. Rosenthal PB, Henderson R. Optimal determination of particle orientation, absolute hand, and contrast loss in single-particle electron cryomicroscopy. Journal of molecular biology. 2003; 333:721–745. [PubMed: 14568533]
29. Holm L, Rosenstrom P. Dali server: conservation mapping in 3D. Nucleic acids research. 2010; 38:W545–549. [PubMed: 20457744]
30. Kurakawa T, et al. Direct control of shoot meristem activity by a cytokinin-activating enzyme. Nature. 2007; 445:652–655. [PubMed: 17287810]
31. Baugh L, et al. Increasing the structural coverage of tuberculosis drug targets. Tuberculosis. 2015; 95:142–148. [PubMed: 25613812]
32. Jin P, et al. Electron cryo-microscopy structure of the mechanotransduction channel NOMPC. Nature. 2017; 547:118–122. [PubMed: 28658211]
33. Ullrich ND, et al. Comparison of functional properties of the Ca2+-activated cation channels TRPM4 and TRPM5 from mice. Cell calcium. 2005; 37:267–278. [PubMed: 15670874]
34. Demeuse P, Penner R, Fleig A. TRPM7 channel is regulated by magnesium nucleotides via its kinase domain. The Journal of general physiology. 2006; 127:421–434. [PubMed: 16533898]
35. Zhang Z, et al. The TRPM6 kinase domain determines the Mg.ATP sensitivity of TRPM7/M6 heteromeric ion channels. The Journal of biological chemistry. 2014; 289:5217–5227. [PubMed: 24385424]
36. N ER Jr. Phenomenological Theory of Ion Solvation. Effective Radii of Hydrated Ions. J Phys Chem. 1959; 63:1381–1387.
37. Nilius B, et al. The selectivity filter of the cation channel TRPM4. The Journal of biological chemistry. 2005; 280:22899–22906. [PubMed: 15845551]
38. Long SB, Tao X, Campbell EB, MacKinnon R. Atomic structure of a voltage-dependent K+ channel in a lipid membrane-like environment. Nature. 2007; 450:376–382. [PubMed: 18004376]

39. Payandeh J, Scheuer T, Zheng N, Catterall WA. The crystal structure of a voltage-gated sodium channel. Nature. 2011; 475:353–358. [PubMed: 21743477]
40. Guo J, et al. Structure of the voltage-gated two-pore channel TPC1 from Arabidopsis thaliana. Nature. 2016; 531:196–201. [PubMed: 26689363]
41. Yamaguchi S, Tanimoto A, Otsuguro K, Hibino H, Ito S. Negatively charged amino acids near and in transient receptor potential (TRP) domain of TRPM4 channel are one determinant of its Ca2+ sensitivity. The Journal of biological chemistry. 2014; 289:35265–35282. [PubMed: 25378404]
42. Liao M, Cao E, Julius D, Cheng Y. Structure of the TRPV1 ion channel determined by electron cryo-microscopy. Nature. 2013; 504:107–112. [PubMed: 24305160]
43. Paulsen CE, Armache JP, Gao Y, Cheng Y, Julius D. Structure of the TRPA1 ion channel suggests regulatory mechanisms. Nature. 2015; 525:552.
44. Gao Y, Cao E, Julius D, Cheng Y. TRPV1 structures in nanodiscs reveal mechanisms of ligand and lipid action. Nature. 2016; 534:347–351. [PubMed: 27281200]
45. Goehring A, et al. Screening and large-scale expression of membrane proteins in mammalian cells for structural studies. Nature protocols. 2014; 9:2574–2585. [PubMed: 25299155]
46. Denisov IG, Grinkova YV, Lazarides AA, Sligar SG. Directed self-assembly of monodisperse phospholipid bilayer Nanodiscs with controlled size. Journal of the American Chemical Society. 2004; 126:3477–3487. [PubMed: 15025475]
47. Zheng SQ, et al. MotionCor2: anisotropic correction of beam-induced motion for improved cryo-electron microscopy. Nature methods. 2017; 14:331–332. [PubMed: 28250466]
48. Zhang K. Gctf: Real-time CTF determination and correction. Journal of structural biology. 2016; 193:1–12. [PubMed: 26592709]
49. Scheres SH. RELION: implementation of a Bayesian approach to cryo-EM structure determination. Journal of structural biology. 2012; 180:519–530. [PubMed: 23000701]
50. Bai XC, Rajendra E, Yang G, Shi Y, Scheres SH. Sampling the conformational space of the catalytic subunit of human gamma-secretase. eLife. 2015; 4
51. Kucukelbir A, Sigworth FJ, Tagare HD. Quantifying the local resolution of cryo-EM density maps. Nature methods. 2014; 11:63–65. [PubMed: 24213166]
52. Emsley P, Lohkamp B, Scott WG, Cowtan K. Features and development of Coot. Acta crystallographica. Section D, Biological crystallography. 2010; 66:486–501. [PubMed: 20383002]
53. Adams PD, et al. PHENIX: a comprehensive Python-based system for macromolecular structure solution. Acta crystallographica. Section D, Biological crystallography. 2010; 66:213–221. [PubMed: 20124702]
54. DiMaio F, Zhang J, Chiu W, Baker D. Cryo-EM model validation using independent map reconstructions. Protein science : a publication of the Protein Society. 2013; 22:865–868. [PubMed: 23592445]
55. Amunts A, et al. Structure of the yeast mitochondrial large ribosomal subunit. Science. 2014; 343:1485–1489. [PubMed: 24675956]
56. Chen VB, et al. MolProbity: all-atom structure validation for macromolecular crystallography. Acta crystallographica. Section D, Biological crystallography. 2010; 66:12–21. [PubMed: 20057044]
57. Smart OS, Neduvelil JG, Wang X, Wallace BA, Sansom MS. HOLE: a program for the analysis of the pore dimensions of ion channel structural models. Journal of molecular graphics. 1996; 14376:354–360. [PubMed: 9195488]
58. Schrödinger L. The PyMOL Molecular Graphics System. Version 1.8. 2015
59. Pettersen EF, et al. UCSF Chimera–a visualization system for exploratory research and analysis. Journal of computational chemistry. 2004; 25:1605–1612. [PubMed: 15264254]

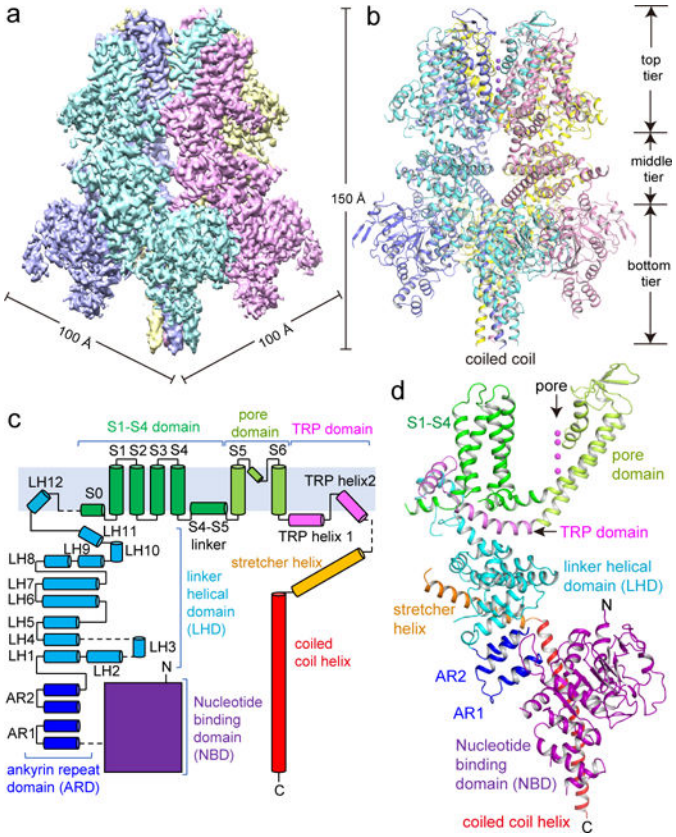

Figure 1.

Overall structure of TRPM4. **a**, 3D reconstruction of TRPM4 with each subunit in individual color. **b**, Cartoon representation of TRPM4 structure depicting the three-tiered architecture. **c**, Schematic representation of the domain arrangement in a single TRPM4 subunit. **d**, Structure of a single subunit in the same orientation as the cyan-colored subunit in **b**, Domains are individually colored in **c** and **d**.

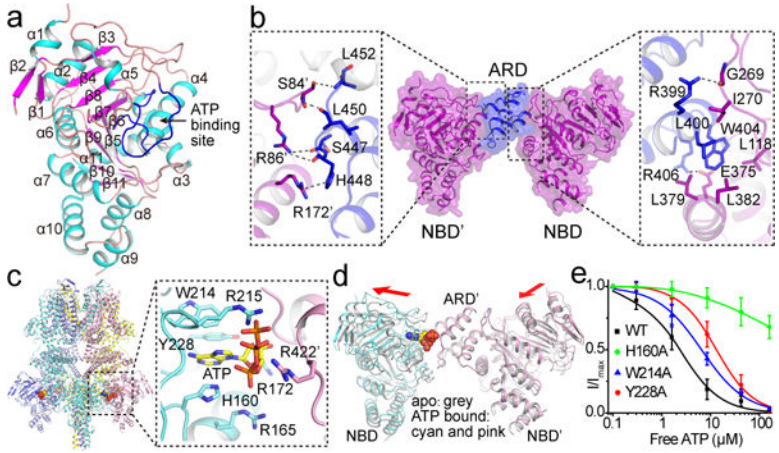

Figure 2.

Bottom-tier NBD and ARD. **a**, Structure of NBD. Loops colored in blue form the ATP binding pocket. **b**, Side view of tetrameric assembly of NBD (purple) and ARD (blue). Insets are zoomed-in views of inter-domain interactions between NBD and ARD within the same subunit (right inset) and from two neighboring subunits (left inset). Hydrogen bonds and salt bridges are indicated by dotted lines. **c**, ATP binding at NBD with zoomed-in view of the binding pocket. **d**, Superposition of TRPM4 structures at the bottom tier NBD/ARD region in the apo (grey) and ATP- bound (pink and cyan with ATP in CPK model) forms. Arrows mark the directions of rigid-body movement of NBD upon ATP binding. **e**, Concentration dependent free ATP inhibition of wild-type and mutant TRPM4 channels. Data are reported as mean ± SEM of five independent biological replicates (source data in Supplementary Information). Curves are least square fits to Hill equation (except H160A) with IC_{50} of 2.3±0.5, 6.5±0.8 and 14.2±0.7 μM, and Hill coefficient n of 1.05±0.09, 0.96±0.08 and 1.16±0.07 for wild type, W214A and Y228A, respectively. The IC_{50} of H160A is larger than 160 μM.

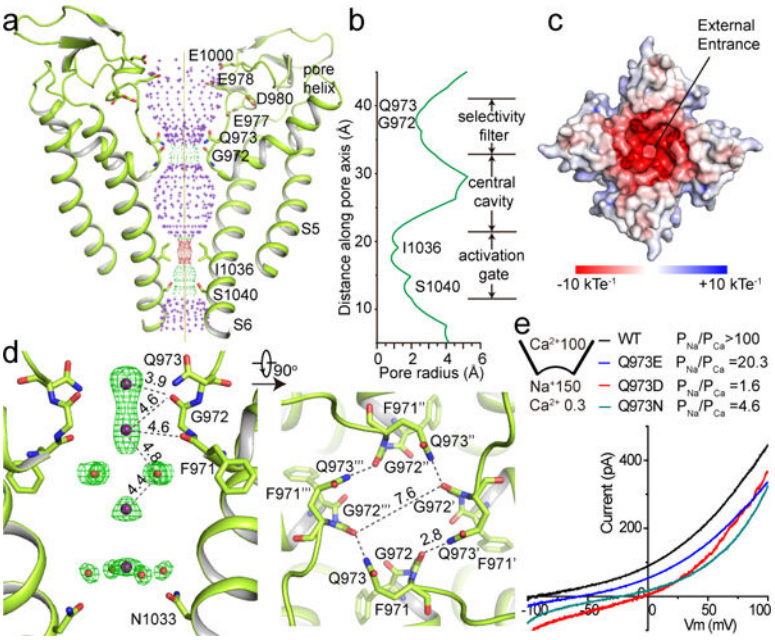

Figure 3.

Ion conduction pore and channel selectivity. **a**, Ion conduction pore of TRPM4 with front and rear subunits removed for clarity. Central pathway is marked with dotted mesh. **b**, Pore radius along the central axis. **c**, Surface electrostatic potential at the external entrance of TRPM4. **d**, Zoomed-in view of the selectivity filter with atom-to-atom distances in Å. EM density peaks in the filter region are modeled as Na^+ (purple sphere) and water (red sphere). **e**, Relative permeability (P_{Na}/P_{Ca}) between Na^+ and Ca^{2+} in the wild-type and mutant channels. Shown are sample I-V curves recorded with 100 mM Ca^{2+} in pipette, 150 mM Na^+ and 0.3 mM Ca^{2+} in bath. P_{Na}/P_{Ca} values are calculated from the reversal potentials (mean ± SEM of five independent biological replicates in mV): −97.5±8.6 for WT, −55.2±6.3 for Q973E, −4.1±2.4 for Q973D and −23.6±4.5 for Q973N.

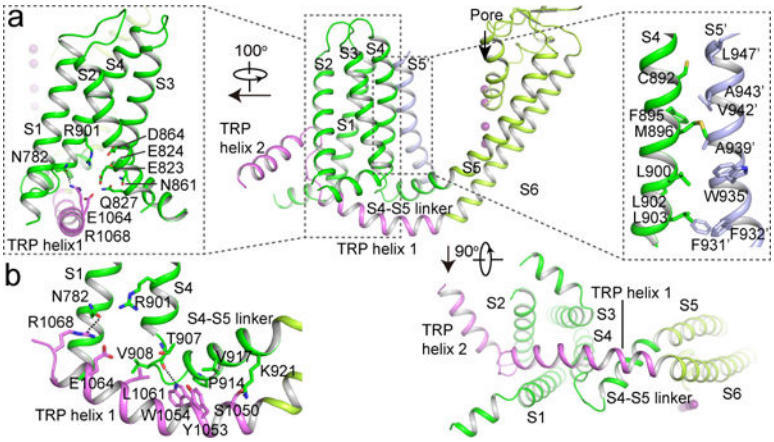

Figure 4.

S1-S4 and TRP domains. **a**, Side view (middle) and intracellular view (bottom) of a single subunit of the top-tier transmembrane region with S1-S4 in green and TRP domain in pink. Left inset shows the helical packing within S1-S4 and the intracellular cavity. Right inset shows the hydrophobic packing between S4 and S5 of neighboring subunit (S5′ in light blue). **b**, Interactions between TRP helix 1 and the S4-S5 linker.

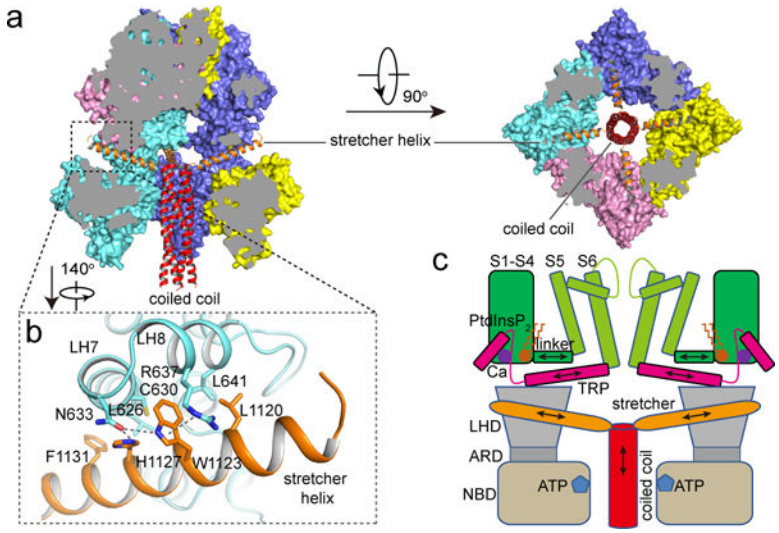

Figure 5.

C-terminal stretcher and coiled-coil helices. **a**, Structures of the stretcher helices (orange) and the four-helix coiled coil (red) in the context of the channel (surface rendered model). The front section of the channel is removed for clarity. **b**, Zoomed-in view of the contact between the stretcher helix and LH7-8 of LHD. **c**, Cartoon representation of TRPM4 gating machinery. Arrows indicate the potential movements that can regulate the channel gating.